Identifying Dynamic Response of a Twenty-Story Instrumented Building to 2018 M7.1 Anchorage, Alaska Earthquake and Its Aftershocks

Weiping Wen & Erol Kalkan

Published online: 19 Oct 2021.

Submit your article to this journal

Article views: 19

View related articles

View Crossmark data

Taylor & Francis
Taylor & Francis Group

Check for updates

Identifying Dynamic Response of a Twenty-Story Instrumented Building to 2018 M7.1 Anchorage, Alaska Earthquake and Its Aftershocks

Weiping Wen [a] and Erol Kalkan[b]

aKey Lab of Structures Dynamic Behavior and Control of the Ministry of Education, Harbin Institute of Technology, Harbin, China; bQuakeLogic Inc., Roseville, California, USA

ABSTRACT

The dynamic responses of an instrumented twenty-story steel-moment frame office building were identified with the data from mainshock (M 7.1) occurred on November 30, 2018 and its six aftershocks ranging from M4.2 to 5.7 in the Alaska-Aleutian subduction zone. The deconvolution-based seismic interferometry was used to identify the traveling waves and intrinsic-damping ratio in the building. The median shear-wave velocity is 179 m/s for the east-west (EW), 201 m/s for the north-south (NS), and 174 m/s for the torsional responses. The building's average intrinsic-damping ratio is estimated to be 4.4% and 3.7% for the EW and NS directions, respectively.

1. Introduction

In 2003, Robert B. Atwood Building in Anchorage, Alaska (a twenty-story regular-plan steel-moment frame office building) is instrumented with a 32-channel accelerometer array at ten levels by the US. Geological Survey (USGS). The buil-`+*ding instrumentation is accompanied by a free-field station and downhole geotechnical array located in Delaney Park. This secondary seismic array, 180 m away from the Atwood building, aims to measure soft sediments' response to earthquake shaking and provide input wavefield data. The photo of the building and nearby Delaney Park seismic stations is presented in Fig. 1.

The Atwood building experienced the 2018 M7.1 Anchorage earthquake and its aftershocks. The mainshock is the largest earthquake impacted Anchorage following the devastative M9.2 great Alaskan earthquake of 1964. We examined the wave-propagation in this building during the 2018 earthquake sequence, and determined its dynamic response characteristics. The deconvolution-based seismic interferometry was used to model the wave propagation in the building for tracking the changes (if any) in the structure's stiffness. This method is advantageous over cross-correlation-based interferometry because it considers the correlation of motions at different observation points and changes the base's boundary condition (Wen and Kalkan 2017). The structural response can be recovered using impulse response functions (IRFs) regardless of its coupling to the subsurface (Kohler, Heaton, and Bradford 2007; Snieder and Şafak 2006; Vasconcelos and Snieder 2008) provided that no rocking takes place at the foundation level (Ebrahimian and Todorovska 2014, 2015; Rahmani, Ebrahimian, and Todorovska 2015; Todorovska 2009). This method was previously applied to the Atwood building's instrumentation data obtained from earthquakes between 2003 and 2014 (Kalkan and Wen 2017; Wen and Kalkan 2017), and the shear wave velocity profiles and damping values were identified. However, the building's response during these events was relatively small, and the largest peak ground acceleration (PGA) was about 70 cm/s^2. The PGA

Figure 1. Photo showing north façade of twenty-story high Atwood Building next to the Delaney Park borehole array (fenced area) in downtown Anchorage, Alaska (photo = E. Kalkan). The color version of this figure is available only in the electronic edition.

observed in 2018 M7.1 Anchorage mainshock exceeds 200 cm/s^2; thus, it is of interest to re-examine this building's response to the most recent significant earthquake of Anchorage Alaska, and compare them with the previous findings.

2. M7.1 Anchorage Earthquake Sequence

The M7.1 earthquake that occurred in the Alaska-Aleutian subduction zone on November 30, 2018, was caused by east-west tension along with a roughly north-south trending tensional fault within the subducting Pacific slab (Stein, Patton, and Sevilgen 2018). Its epicenter is at about 14 km northwest of downtown Anchorage, Alaska, lying close to the epicenter of the 1964 M9.2 earthquake, which was over a thousand times larger. Earthquakes are common in this region. Besides the above two events, 13 other M6+ earthquakes occurred within 150 km of the 2018 M7.1 event over the past century. The relatively high frequency of earthquakes compared to mainland US also highlights the importance of instrumentation and structural-health-monitoring for the resilience of infrastructure in this region.

The M7.1 earthquake shook Turnagain Arm, and Knik Arm of the Cook Inlet with peak ground accelerations (PGAs) over 1.0 g, and strong shaking peaked at ∼0.30 g throughout much of Anchorage and surrounding areas (Jibson et al. 2020). Although this event did not cause loss of lives or severe injuries, widespread power outages, structural and non-structural damage to public and private buildings were observed (Rodgers et al. 2021; Ruppert and Witter 2020). Besides, many roads experienced severe damage, and liquefaction was significant in severity. The mainshock was followed by a vigorous 10,000 aftershocks reported through the end of July 2019 (Ruppert et al. 2020). In this earthquake sequence, there were nearly 400 felt aftershocks and more than 40 aftershocks with M ≥ 4 (Ruppert and Witter 2020).

3. Description of the Building and Instrumentation

The Atwood Building, located northwest downtown Anchorage Alaska, is an iconic twenty-story moment-resisting steel frame office structure with a basement used as a parking garage. The building was designed according to the 1979 Uniform Building Code (ICBO 1979) and constructed
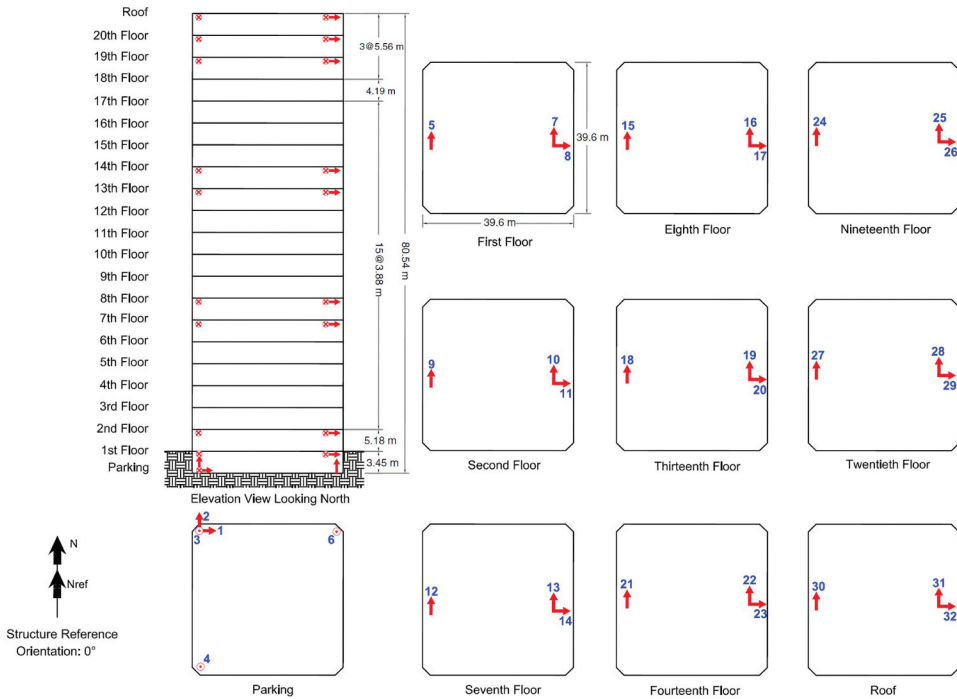
Figure 2. Instrumentation layout of the Atwood Building; arrows indicate sensor orientation; numbers indicate sensor IDs. The height of each floor and a total height of the building from the ground level are shown (see "Data and Resources"). The color version of this figure is available only in the electronic edition.

in 1980. It has a square footprint of 39.6 m (130 ft) with a square concrete core of 14.6 m (60 ft). The total height of the building is 80.54 m (264.2 ft). The building's reinforced concrete shallow foundation consists of a 1.52 m (5 ft) thick mat under the center core with a perimeter wall footing connected with grade beams. The instrumentation consists of a 24-bit IP-based data logger and an array of 32 accelerometers distributed on 10 levels (Fig. 2), including basement, 1st (ground), 2nd, 7th, 8th, 13th, 14th, 19th, 20th, and roof. This accelerometer array records 200 samples-per-second from each channel. Further details on the structure and instrumentation can be found in Wen and Kalkan (2017).

As aforementioned, the M7.1 mainshock and six aftershocks with a magnitude from 4.2 to 5.7 were identified for this study based on their proximity to the building and intensity of recordings. Other distant small aftershocks were discarded due to the low signal-to-noise ratio of their waveforms. The events selected are listed in Table 1, along with origin times, magnitudes, distance, depth, and epicenter coordinates. The epicenters of the selected events are depicted on a regional map in Fig. 3. They are 21–44 km deep and 5.3 to 29.6 km away from the building.

Figure 4 compares horizontal accelerations recorded on the first floor with those at the roof level during these seven earthquakes. The largest peak acceleration of 0.44 g was recorded at the roof during the mainshock at an epicenter distance of 14.3 km. Figure 5 displays the full waveforms in the building's reference east-west direction obtained from this event; the waveforms from the basement amplified as much as 2.1 times at the roof level due to the building's response.

4. Deconvolution

One of the methods to perform the seismic interferometry of two signals is deconvolution. The deconvolution of the response at height z, $u(z, \omega)$ by the response at height z_a, $u(z_a, \omega)$ is defined as

Table 1. Origin times, magnitudes, epicenter locations of main shock and aftershocks recorded by the Atwood building accelerometer array in 2018 Anchorage earthquake sequence.

Event	Origin time (UTC) (y-m-d, hh:mm:ss)	Magnitude	Epicenter Coordinates		Depth (km)	Epicenter Distance (km)	Peak Acceleration (cm/s²)	
			Lat. (°)	Long. (°)			Ground	Structure
1	2018/11/30 17:29:29	7.1	61.340	−149.937	40	14.3	233.8	440.2
2	2018/11/30 17:33:52	4.8	61.363	−149.880	44	16.7	41.4	79.1
3	2018/11/30 17:35:37	5.7	61.259	−149.921	39	5.3	41.4	78.9.
4	2018/11/30 17:43:00	4.5	61.516	−149.908	41	33.7	8.7	8.2
5	2018/11/30 19:26:30	4.9	61.394	−149.972	38	20.5	13.3	15.8
6	2018/11/30 20:26:56	5.1	61.392	−150.064	31	21.9	17.5	33.7
7	2018/11/30 23:07:47	4.2	61.472	−150.026	21	29.6	2.9	4.7

The earthquakes are numbered sequentially according to their origin times. Peak acceleration is the observed absolute maximum amplitude of the waveforms from the accelerometers at the ground and roof floors. Event 1 is the mainshock, and events 2–7 are six selected aftershocks.
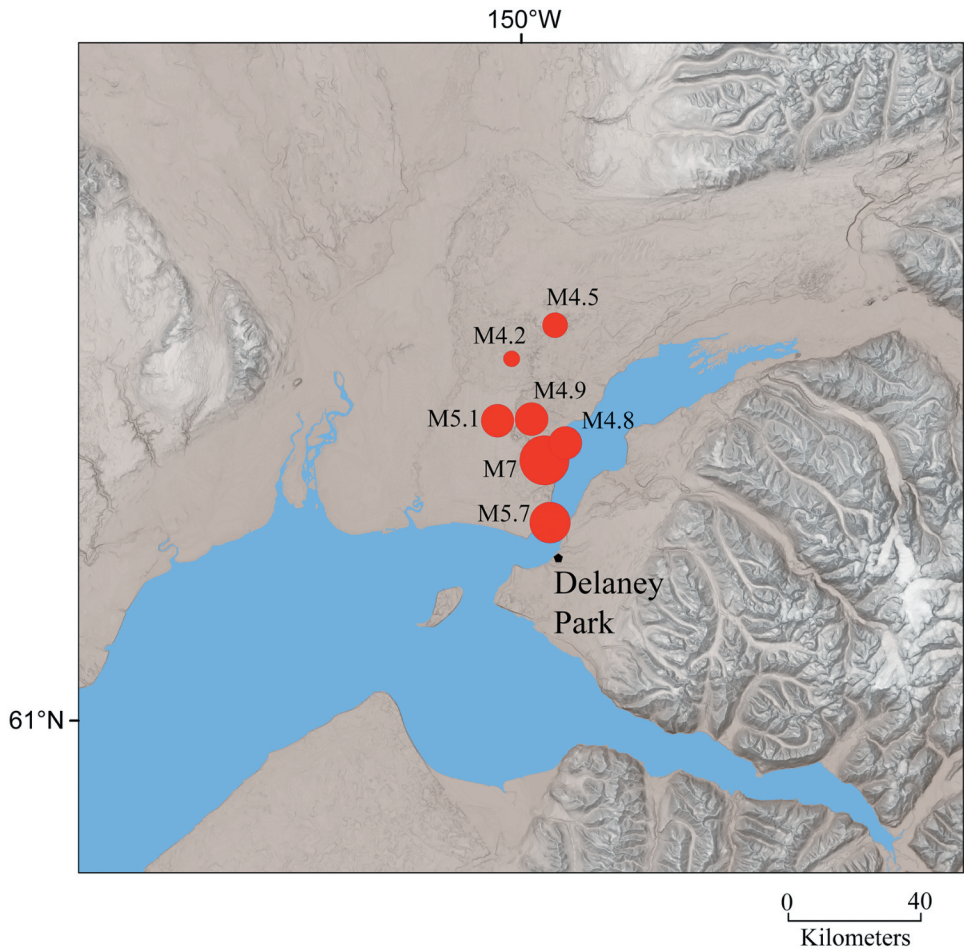
Figure 3. Map showing the location of the Atwood Building (Delaney Park, N61.21528° and W149.89296°) and epicenters of selected mainshock and aftershocks with circles (summarized in Table 1) [**M** = moment magnitude] (see "Data and Resources"). The color version of this figure is available only in the electronic edition.
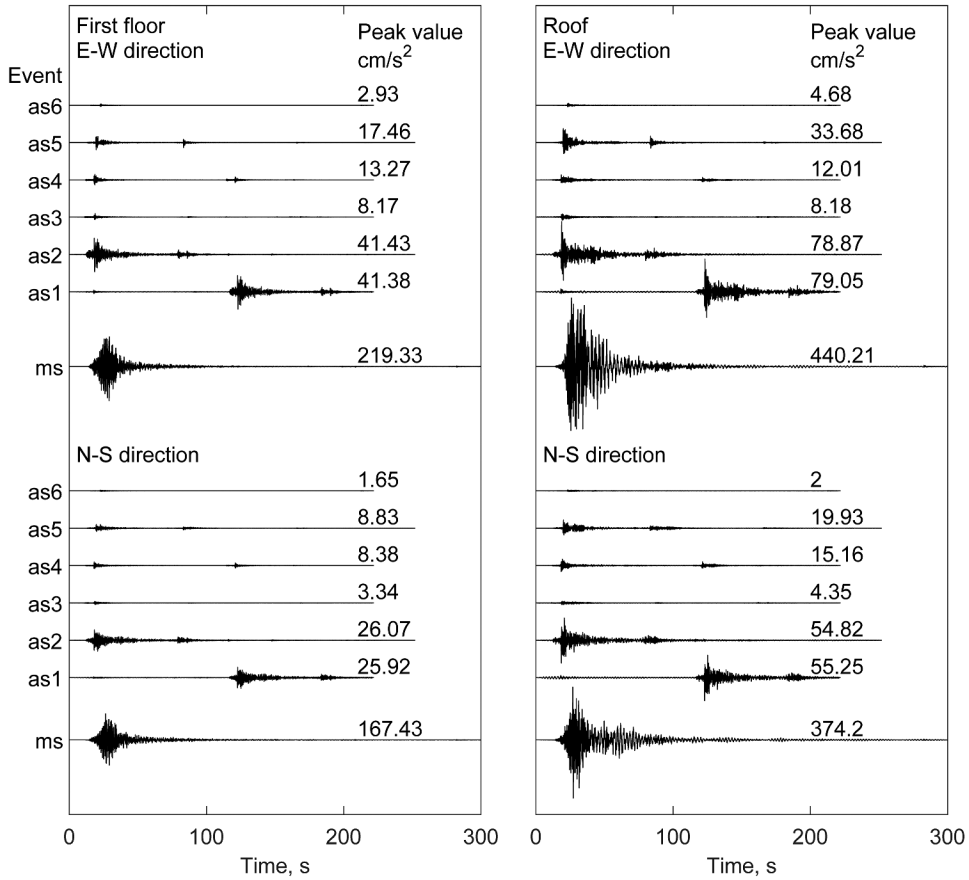
Figure 4. Horizontal acceleration waveforms recorded at first-floor and roof level during seven earthquakes summarized in Table 1.

$$D(z, z_a, \omega) = u(z, \ \omega)/u(z_a, \ \omega) \tag{1}$$

The above equation may become ill-conditioned when the denominator approaches zero. Thus, the following regularized format is used as the estimator of deconvolution:

$$D(z, z_a, \omega) = [u(z, \ \omega)u^*(z_a, \ \omega)]/\big[|u(z_a, \ \omega)|^2 + \varepsilon\langle|u(z_a, \ \omega)|^2\rangle\big] \tag{2}$$

where superscript "*" denotes the complex conjugate, ε is the regularization parameter (ε=0.01 is used here), $\langle|u(z_a, \ \omega)|^2\rangle$ is the average power spectrum of $u(z_a, \ \omega)$.

5. Results

The deconvolution was applied to the horizontal components of waveforms recorded in the building. The structural responses $u(z, \omega)$ from instrumented floors were deconvolved by the structural response measured at the roof $u(H, \omega)$. Full lengths of the waveforms were used because the building's response remained essentially elastic (will be discussed later). The deconvolved waveforms (i.e. IRFs) were bandpass filtered with corner frequencies of 0.2 and 8 Hz using a second-order acausal (zero phase-shift) Butterworth filter to accentuate at least three fundamental modes using recorded motions in EW, NS, and floor torsional motions.
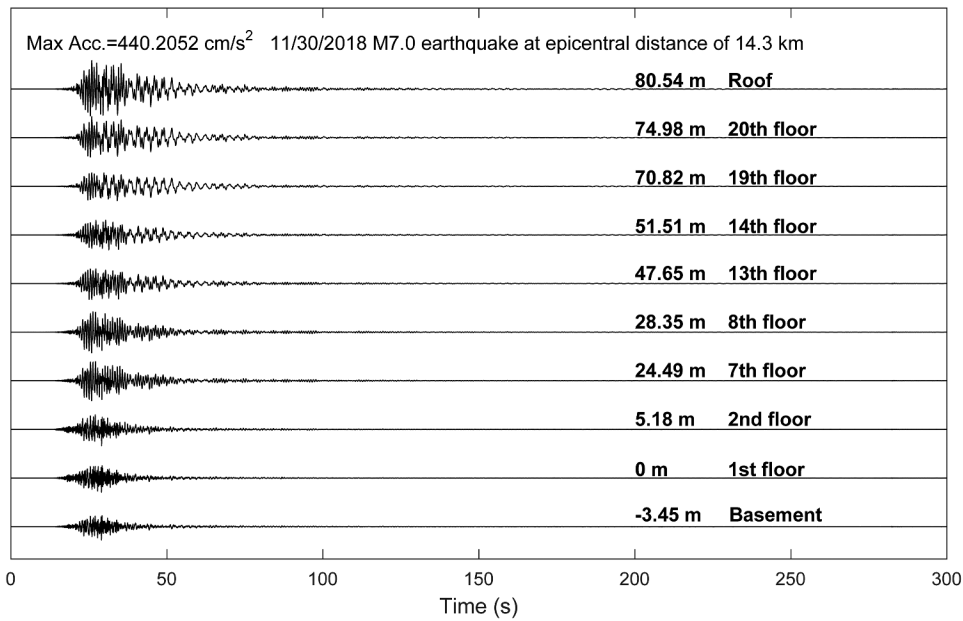
Figure 5. East-west acceleration waveforms from the mainshock at an epicentral distance of 14.3 km. Propagating waves from the basement to the roof show amplification in the order of 2.1. The floor numbers and their corresponding height relative to the ground (1st floor) are depicted; the maximum roof acceleration is 440.2 cm/s².

Figure 6 illustrates the IRFs computed for the EW direction using the waveforms shown in Fig. 5. The IRF at the roof is a bandpass-filtered Dirac delta function (virtual source), and the IRFs across all floors demonstrate a wave state consisting of the response of different parts of the structure to the
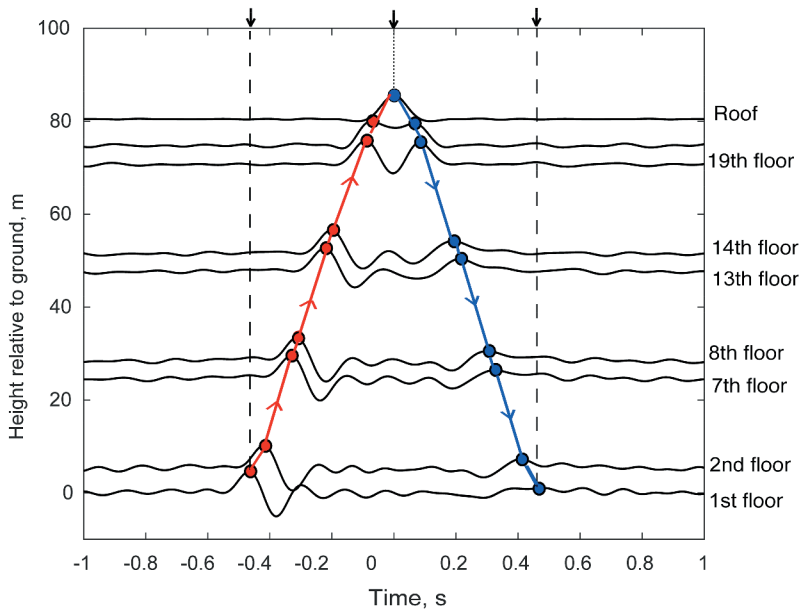

Figure 6. Deconvolved waveforms, calculated from the mainshock east-west direction acceleration time series, are plotted as positive and negative amplitudes for each instrumented floor over time. The frequency range of the waveforms is 0.2–8 Hz. The color version of this figure is available only in the electronic edition.

Dirac delta function at the roof (Nakata and Snieder 2014; Nakata et al. 2013; Nakata, Tanaka, and Oda 2015; Rahmani and Todorovska 2013; Snieder and Şafak 2006). A straightforward wave state, consisting of the superposition of one upward traveling wave (in the negative times) and one downward traveling waves (in the positive times) can be observed. The wave amplitude decay can also be seen by the comparison of amplitudes of the downward and upward traveling waves. For example, in Fig. 6, the amplitudes of the downward traveling waves are generally smaller than the corresponding amplitudes of the upward traveling waves as a result of the damping in the structure.

5.1. Determination of Shear-Wave Velocity and Velocity Profiles

The shear-wave velocity of traveling waves ($V_{S,n}$) for the nth layer between two receivers can be derived considering the time lag τ between peaks of IRFs and the travel distance following the ray theory, which disregards wave scattering (i.e. $V_{S,n} = h/\tau$, where h is the distance in meters). As demonstrated in Fig. 7, a simple three-layer elastic shear-beam according to the receiver locations is used to compute the shear-wave velocity of different layers. The layers, consisting of groups of floors, are assumed to be homogenous, isotropic, perfectly bonded to each other. The assumption on the 3-layer model of the building is based on the sensor locations, and the spatial resolution of the identified results from interferometry (Todorovska and Rahmani 2013).
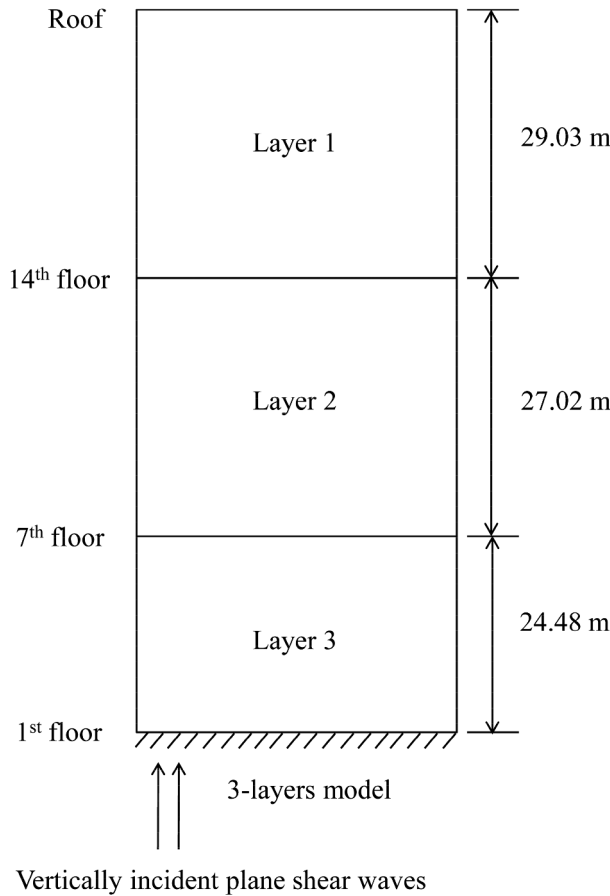
Figure 7. Correspondence between layers and floor numbers for the three-layer shear-beam model used to calculate the average shear-wave velocity of the Atwood Building; heights of each layer are depicted.
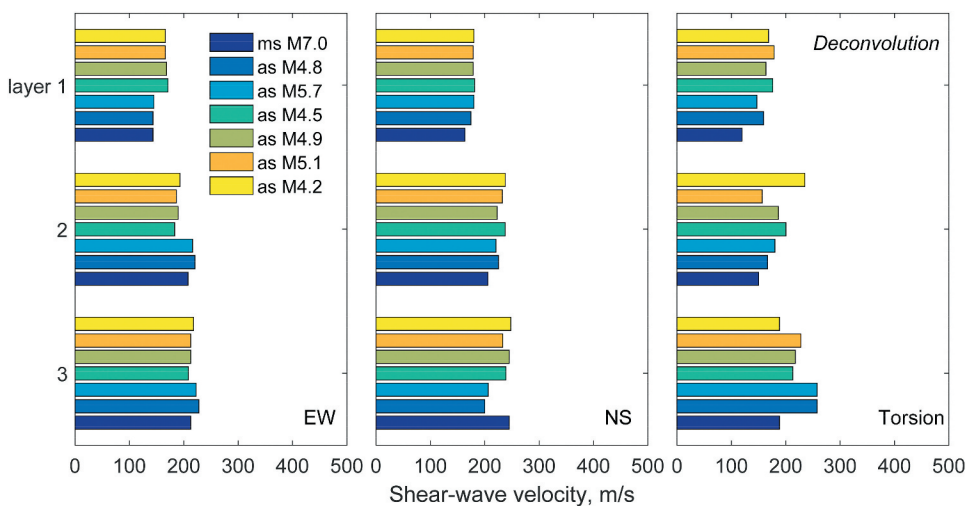
Figure 8. Shear-wave velocity profiles of the Atwood Building for east-west (EW), north-south (NS), and torsional responses considering a three-layer shear-beam model and seven earthquakes. Results are based on deconvolution for the frequency range of 0.2–8 Hz [Layer 1 = upper floors; Layer 3 = lower floors; earthquakes are in ascending order over time]. The color version of this figure is available only in the electronic edition.

The shear-wave velocities of upward and downward traveling waves are averaged. Figure 8 shows the shear-wave velocity profiles for the EW, NS, and floor torsional motions considering seven earthquakes for the frequency range of 0.2–8 Hz. The results in Fig. 8 are shown following the order of occurrence times of mainshock and six aftershocks. For the N-S direction, the records from the accelerometer on the same side are firstly used to obtain the dynamic properties of the building, and then the results of the dynamic properties from the two sides are averaged. The normalized difference between the two accelerations in the N-S component by the distance of two accelerometers is used as the torsional responses, and then the seismic interferometry method is applied to the torsional responses to obtain the torsional properties of the building. Similar to the earlier earthquakes (Wen and Kalkan 2017), the general reduction of shear-wave velocity from the base to the top can be observed in the three directions. However, the shear-wave velocity of layer 3 (i.e. the base part of the building) is slightly lower than that obtained from the earlier events in two translational directions, which may be due to the recoverable non-structural damage induced by this earthquake sequence.

The median and standard deviation of shear-wave velocity distributions along with the height of the structure, determined using the deconvolution from all events considering the EW, NS, and floor torsional motions, are compared next in Fig. 9. The median velocity for different layers and directions are generally comparable with those obtained from the earlier events (from 2003 to 2014), except the velocity of layer 3 for the EW and NS directions, which is slightly lower than the corresponding velocity from the earlier earthquakes. The variation of velocities is also similar with previous results, and the velocities in torsional direction still show higher dispersion than that those in the EW and NS directions.

We also determined the median shear-wave velocity of the entire building using the three-layer shear-beam model. An example is shown in Fig. 10 for the records shown in Fig. 5. The record on the 1st floor is shown in Fig. 10a. To track the evolution of the shear-wave velocity, the entire record from this event (i.e. mainshock) is divided into three parts: strong-motion part (10–110 s), coda wave part-I (110–210 s) and coda wave part-II (210–310 s). The corresponding IRFs are shown in Fig. 10b. In Fig. 10c, the square and circular marks correspond to the time of the peaks in the IRFs, similar to those portrayed in Figs. 6 and 10b. The travel distance is measured relative to the position of the virtual source (i.e. roof). The negative travel distance is for an upward traveling wave. A straight line was fitted
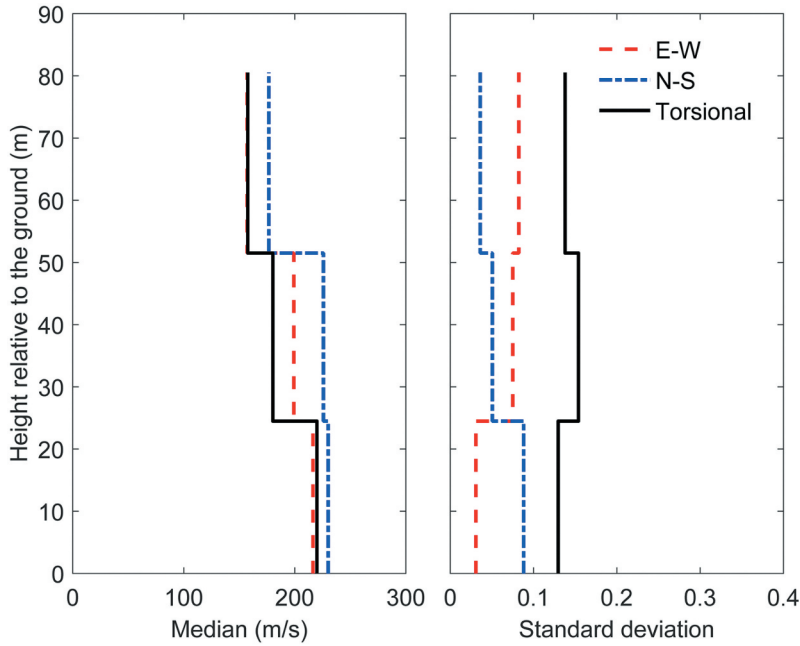
Figure 9. Median and variability of shear-wave velocity based on the three-layer shear-beam model considering seven earthquakes. The color version of this figure is available only in the electronic edition.
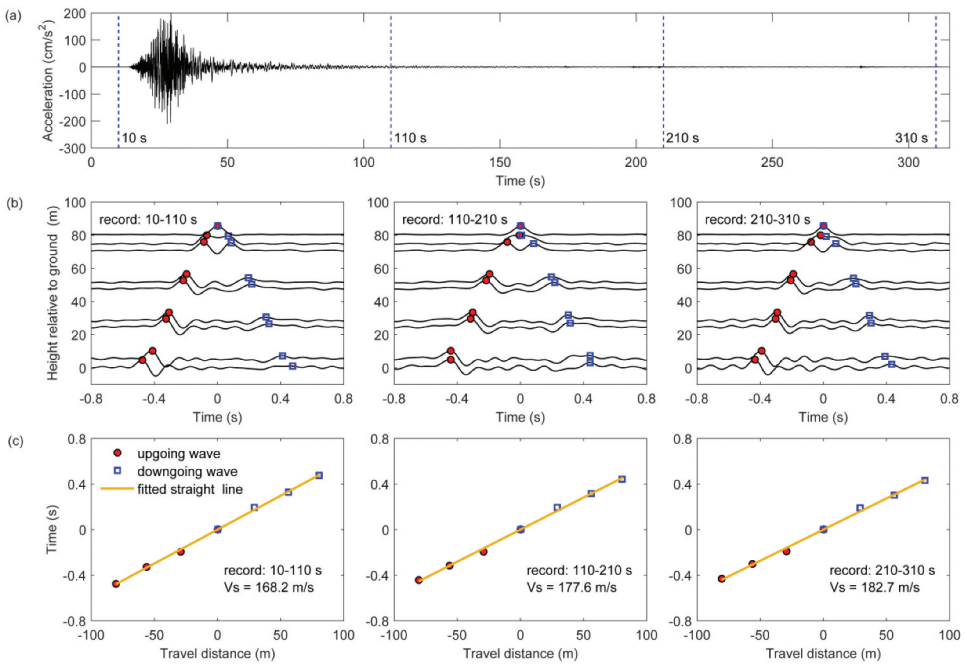
Figure 10. Deconvolution results for different parts of the mainshock records: (a) the entire recording of the mainshock ground motion, and it is divided into three parts [strong motion part, and coda wave part I and II]; (b) deconvolved waveforms by using the different parts of the mainshock records; (c) a straight line is fitted to all data points by least squares to determine the average shear-wave velocity in the building. The color version of this figure is available only in the electronic edition.

Table 2. Shear-wave velocity of the Atwood building based on deconvolution.

Direction	Event No.							Median
	1	2	3	4	5	6	7	
East-west	172.9	177.7	177.3	181.3	182.8	180.4	183.2	179.3
North–south	189.1	194.6	197.6	208.2	203.2	204.3	208.6	200.7
Torsional	139.2	174.3	172.1	190.3	179.7	177.1	191.3	174.1

Unit is m/s.

to the distance and time pairs identified from the upward and downward traveling waves using least squares. The shear-wave velocity of the entire building shown in Fig. 10c is 168.2 m/s, 177.6 m/s, and 182.7 m/s for the strong motion part, coda wave part-I and coda wave part-II, respectively. The variation of shear-wave velocities obtained from different windows of the record is within 9%, indicating that no structural damage occurred during the mainshock.

In light of the above discussion, the full length of the record is used to compute the shear-wave velocity of the entire building, and the resultant shear-wave velocities are listed in Table 2 for all events. The median shear-wave velocities along the NS direction are in general 10% larger than those along the EW direction because the averaged stiffness of the building along the NS direction is slightly larger than that along the EW direction. The variation of shear-wave velocity can be observed for various earthquakes. The results of the seven earthquakes are generally stable, and the variation of shear-wave velocities for different events are within 10% for the EW and NS directions. Except for the mainshock, the variation of shear-wave velocities for various events are also within 10% for torsional direction.

The median shear-wave velocities of different four events before 2014 are 191, 205.2, and 176.3 m/s for EW, NS, and torsional directions, respectively (Wen and Kalkan 2017). The results in Table 2 indicate that median shear-wave velocities of different seven events in this earthquake sequence are 179.3, 200.7 m/s, and 174.1 m/s for EW, NS, and torsional directions, respectively. The differences of median shear-wave velocities among two group events are generally within 7%, indicating that the structural responses of this building generally remained in the elastic range during the events from 2005 to 2018.

5.2. Computation of Predominant Frequencies and Mode Shapes

The shear-wave velocity is related to the stiffness and strength of the building, and the decrease in shear-wave velocity may indicate a change in stiffness and/or strength. Therefore, it can be effectively used in conjunction with the modal analyses results. The predominant frequency (f) of a homogenous isotropic

Table 3. Building vibration frequencies identified by the wave propagation method [$V_S/(4 H)$] and the complex mode indicator function for mode-1, mode-2, and mode-3 by using recorded horizontal motions in the building along east-west and north-south directions as well as inferred floor torsional motions.

| The direction of Input Motion	Mode Shape		Event No.						
			1	2	3	4	5	6	7
East-West		$V_S/(4 H)$	0.54	0.55	0.55	0.56	0.57	0.56	0.57
	Bending-shear	Mode-1	*0.38*	0.40	0.40	0.46	0.46	0.42	0.48
	Bending-shear	Mode-2	*1.26*	1.28	1.28	1.43	1.42	1.39	1.45
	Torsion	Mode-3	*2.53*	2.53	2.53	2.72	2.72	2.65	2.73
North-South		$V_S/(4 H)$	0.59	0.60	0.61	0.65	0.63	0.63	0.65
	Bending-shear	Mode-1	*0.44*	0.51	0.51	0.54	0.52	0.52	0.54
	Bending-shear	Mode-2	*1.60*	1.64	1.64	1.75	1.67	1.73	1.79
	Torsion	Mode-3	*2.51*	2.49	2.49	2.70	2.67	2.61	2.82
Torsional		$V_S/(4 H)$	0.43	0.54	0.53	0.59	0.56	0.56	0.59
	Bending-shear	Mode-1	0.43	0.44	0.44	0.60	0.56	0.56	0.60
	Bending-shear	Mode-2	1.25	1.33	1.33	1.43	1.43	1.43	1.67
	Torsion	Mode-3	2.55	2.51	2.51	2.72	2.70	2.58	2.84

Unit is Hz (mode shapes of frequencies italicized are shown in Fig. 12).

shear-beam can be simply estimated from the shear-wave velocity (V_s) (i.e. $f = V_s/4H$ where H is the total height). The predominant frequency derived by this simple formula is presented in Table 3 for the EW, NS, and torsional directions. For comparison, the predominant frequency of the structure is also estimated with the complex mode indicator function (CMIF), which is based on the singular value decomposition of multiple reference frequency response functions (FRFs) (Shih et al. 1988). The FRF is computed as

$$H(f) = P_{xx}(f)/P_{xy}(f) \tag{3}$$

where P_{xx} is the power spectral density of the structural response measured at the roof, and P_{xy} is the cross power spectral density of the structural response measured at the roof and at the first floor. Note that Eq. (3) is inverted compared to most uses of this method (Rades 2010). A detailed review of the CMIF can be found in Allemang and Brown (2006).

Figure 11 presents the typical CMIF curves for the EW, NS, and torsional directions with the records from mainshock and six aftershocks. The largest singular values have peaks at the damped natural frequencies. Therefore, the first three predominant frequencies can easily be detected from the CMIF for the EW and NS and torsional responses. Those identified frequencies are also listed in Table 3. We extracted the first three fundamental modes of the building independently using the recorded motions in the EW and NS directions, as well as by using the floor torsional motions. While the first two modes correspond to bending-shear, the third mode is torsion. The frequencies identified with mainshock records are generally lower than those identified with aftershock records, and this phenomenon is consistent with the shear-wave velocity results in Table 2. For the seven earthquakes, the relative difference between the largest and lowest predominant frequencies is 26% for the translational and
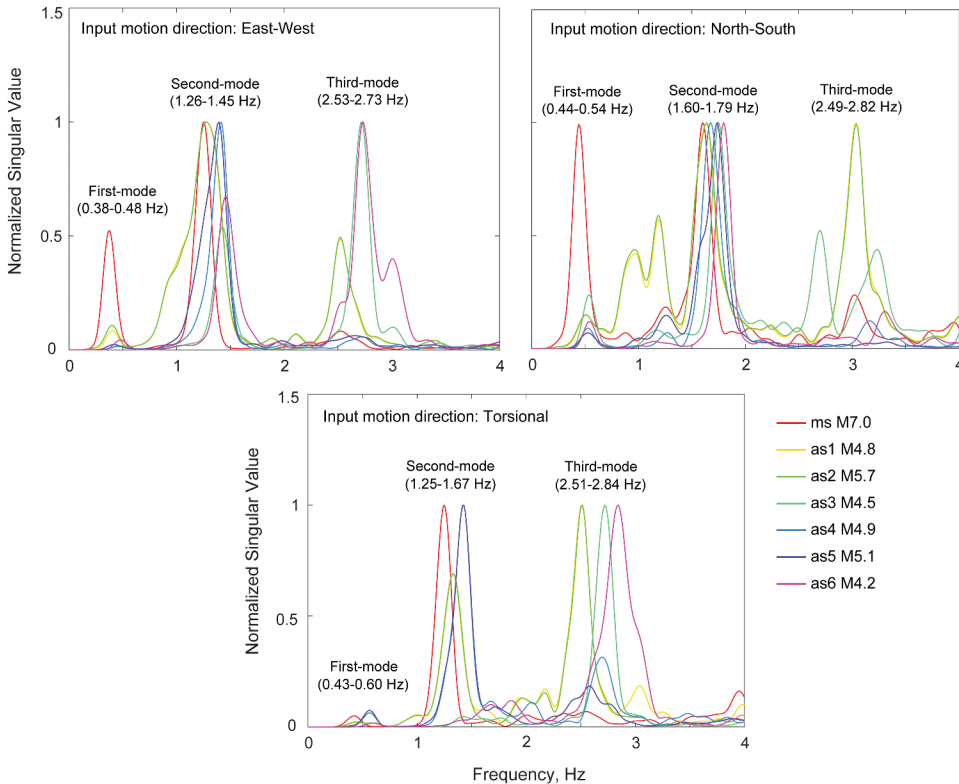

Figure 11. The first three fundamental mode frequencies were identified in east-west (EW), north-south (NS), and torsional responses by complex mode indicator function using the waveform data from seven earthquakes (listed in Table 1). The color version of this figure is available only in the electronic edition.

39% for the torsional response. The relative differences between the largest and lowest second- and the third-mode frequencies are within 15% of the translational directions and up to 34% of the torsion. The variation of frequencies is moderately higher than those identified with the events from 2005 to 2014 (Wen and Kalkan 2017), mainly due to the strong ground motion induced by the mainshock.

The frequencies corresponding to events 1–3 (i.e. mainshock and first two strong aftershocks) are generally comparable, while those corresponding to events 4–7 (i.e. 3rd aftershock to 7th aftershock) are generally similar. The median of former frequencies is lower than those of latter frequencies by about 15% for the translational and 33% for the torsional response. The average value of the fundamental frequency (first-mode) from seven earthquakes is 0.43, 0.51, and 0.52 Hz, respectively, for the EW, NS, and torsional responses.

The predominant frequencies are primarily for the fix-based structure because no rocking took place at the foundation level during any earthquakes. The average ratios of the second-and third-mode frequencies to the first-mode frequency are generally close to the characteristics of the analytical shear-beam, having the frequency ratio of 1:3:5. For example, the ratios are 1:3.3:6.7 for the EW response, 1:3.6:5.7 for the NS response, and 1:2.9:5.9 for the torsional response for the mainshock. If these ratios alter significantly from the analytical ratios, there would be a need to include bending deformations in addition to shear deformations (Boutin et al. 2005; Ebrahimian and Todorovska 2015).

The first six mode shapes and their frequencies are illustrated in Fig. 12 using the waveform data of the mainshock. The mode shapes corresponding to 0.38 and 0.44 Hz are the first bending-shear modes in the EW and NS directions, respectively. The modes with 1.26 and 1.60 Hz are the second bending-shear mode in EW and NS directions, respectively. The modes with 2.53 and 2.51 Hz are essentially the same torsional mode obtained separately by analyzing the EW and NS direction recorded motions separately. In the left three panels, the blue curves with diamond indicate the mode shape in EW direction, while the red curves with circle reflect the effects of NS direction on the mode shape in EW direction (i.e. this curve closes to the vertical line indicate no coupling between the mode shape of two directions). In the right three panels, the red curves with a circle indicate the mode shape in the NS direction. The first bending-shear modes (in the EW or NS direction) are very close to the analytical solution of the shear beam, and no clear coupling can be seen between two translational directions, which is an attribute of the symmetric plan building.
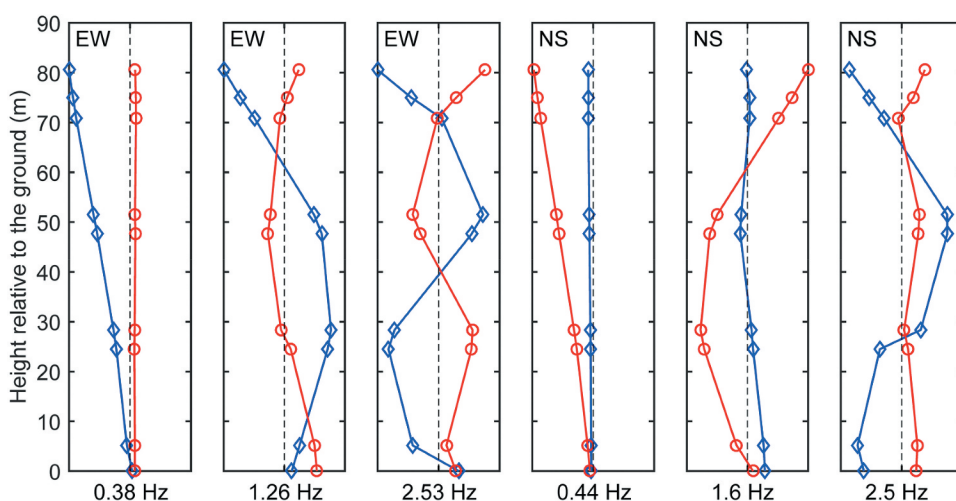

Figure 12. The first six fundamental mode shapes and frequencies are identified by the complex mode indicator function using the waveform data of the mainshock. The color version of this figure is available only in the electronic edition.

5.3. Identifying Changes in Lateral Stiffness

Cladding, roofing, interior walls and ceilings are the non-structural components, which may present notable contributions to the structure's overall lateral stiffness. However, this contribution often diminishes as the excitation intensity amplifies due to the opening of the gaps between non-structural and structural components. Unless there is post-event damage, the gaps close gradually, and non-structural components' contribution to the building's overall lateral stiffness often recovers to its pre-event condition. This is one of the reasons that the aftershocks inducing weaker ground excitations result in building frequencies higher than those resulted due to the strong shaking of the mainshock. The above non-structural damage belongs to the recoverable type, whose effect on the structure's overall lateral stiffness is temporary just during the earthquake. When the non-structural damage becomes more extensive (e.g. wide cracks or even partial collapse occur in the infilled walls), its effect on the structure's overall lateral stiffness would be permanent.

In order to assess whether there is any nonlinearity in the response of the building even at small strains, we plot the roof drift ratio (relative maximum drift between roof and base normalized by the building height) from seven events against the building's first-mode frequencies and median shear-wave velocities using the three-layer shear-beam model along the NS and EW directions considering the seven earthquakes in Fig. 13. This figure clearly shows the trend that as the roof drift ratio increases, the first-mode frequency, and wave-velocity drop. A linear variation trend between first-mode frequencies (or shear-wave velocity) and the logarithm of roof drift can be observed for EW and NS directions. The maximum roof drift is within 0.3% for all the events, indicating again that there is no structural damage occurred in the building.
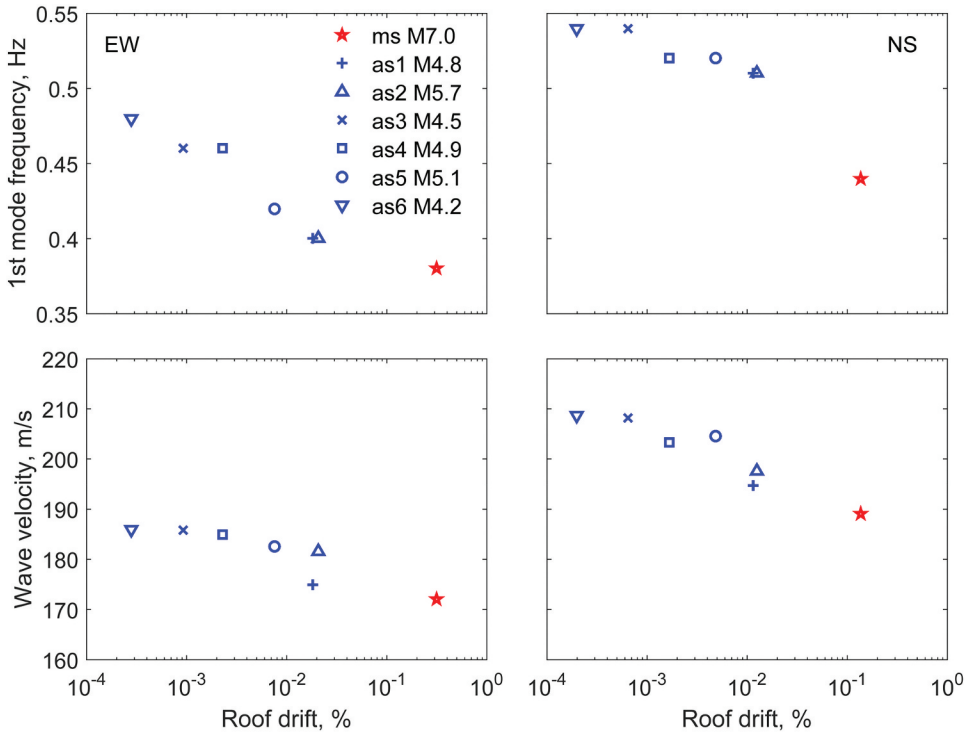
Figure 13. The variation of fundamental frequencies estimated by using the complex mode indicator function (and shear-wave velocities based on three-layer shear-beam model) versus roof drift (given in percentage) for seven earthquakes (listed in Table 1). Roof drift ratio is the maximum absolute roof displacement divided by the building height. X-axes are on a logarithmic scale. The color version of this figure is available only in the electronic edition.

Roux et al. (2014) found that the detection and localization of local perturbations are possible by the analysis of changes in modal frequencies. Instead of time-domain tracking of changes in modal frequencies, we focused on the mode shapes, which represent the deflection patterns of the structure at resonance frequencies, and each component of the mode shape vector carries information corresponding to the location where a motion sensor is placed in the building. To measure the correlation between two sets of mode shape vectors, the modal assurance criterion (MAC) is often used. The MAC provides a single numerical value indicating the correlation between mode shapes (Allemang 2003; Allemang and Brown 1982; Pastor, Binda, and Harčarik 2012). When two mode shapes are fully correlated, the corresponding MAC is 1, whereas fully uncorrelated mode shapes are indicated by a MAC value of 0. The formulation of MAC is

$$\mathrm{MAC}_{mnr} = \frac{\left| \sum_{q=1}^{N_o} \phi_{mqr} \phi_{nqr}^T \right|^2}{\sum_{q=1}^{N_o} \phi_{mqr} \phi_{mqr}^T \sum_{q=1}^{N_o} \phi_{nqr} \phi_{nqr}^T} \tag{4}$$

where ϕ_{mqr} is the modal coefficient for degree-of-freedom q, mode r, and N_o is a number of degrees of freedom. The subscript m indicates the first excitation, and the subscript n denotes the second excitation. Superscript "T" is the transpose operator. Using Eq. (4), the mode shapes identified from each aftershock are compared to those identified from the mainshock. The resultant MAC values, listed in Table 4, demonstrate that the variations in the mode shapes between earthquakes are insignificant as compared to the changes in the frequencies, indicating that no local damage can be identified based on the mode shape. Thus, we attribute reductions in frequencies (and shear-wave velocities) that we observed during the mainshock to the opening and closing of gaps between the non-structural and structural components. Although the nonlinear response of soil, even for weak motion, could affect such variations, the site response of the Atwood building was found to be elastic during these earthquakes based on analyses of waveforms from the nearby geotechnical array in Delaney Park (Kalkan, Wen, and Heo 2021).

5.4. Estimation of Intrinsic Damping

The intrinsic damping can cause energy loss during wave propagation. According to Aki and Richards (2002), it is expressed as:

$$A_s(f) = \exp\left(-\pi \cdot f \cdot \frac{\tau}{Q} \right) \tag{5}$$

where $A_s(f)$ is the reduction in the amplitude of a sinusoidal wave frequency f when it travels a distance of travel time τ, and Q is the quality factor. Earlier studies (Nakata et al. 2013; Newton and Snieder 2012; Prieto et al. 2010; Snieder and Şafak 2006; Wen and Kalkan 2017) utilized this equation together with the IRFs to quantify the intrinsic attenuation in buildings. Because it separates the intrinsic attenuation and radiation damping, the same approach is used here.

Table 4. Modal assurance criterion (MAC) values computed from two sets of mode shape vectors after the main shock (event-1) and after each following aftershock.

Event No.	East-West			North-South		
	Mode-1	Mode-2	Mode-3	Mode-1	Mode-2	Mode-3
2	0.998	0.998	0.909	0.985	1.000	0.935
3	0.998	0.998	0.915	0.984	0.999	0.930
4	0.994	0.998	0.897	0.996	0.988	0.961
5	0.996	0.999	0.914	0.996	0.985	0.853
6	1.000	0.974	0.991	0.987	0.999	0.961
7	1.000	0.995	0.888	0.999	0.998	0.910
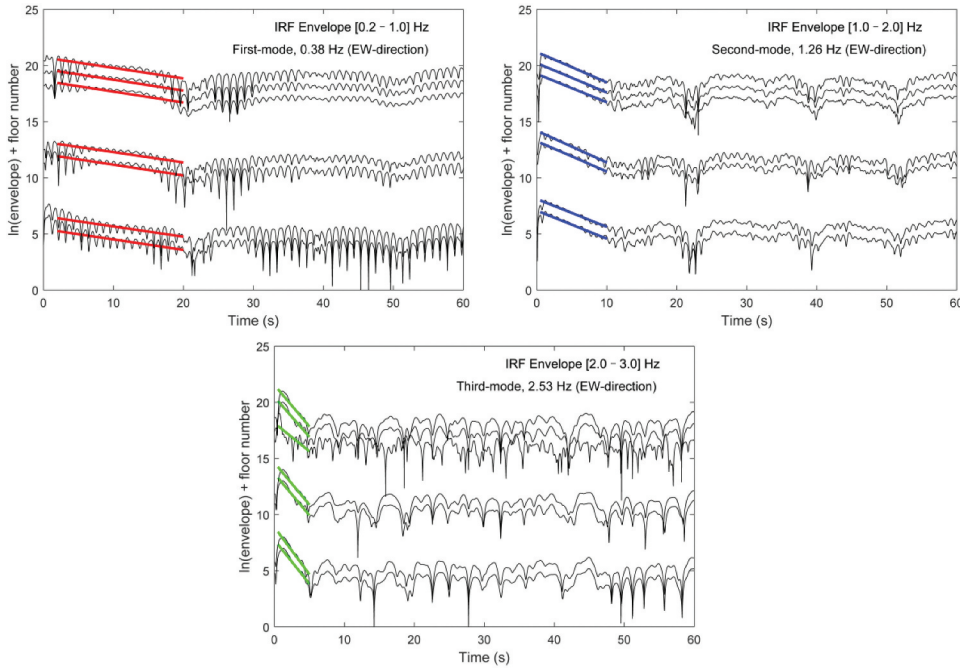
Figure 14. Impulse response functions (IRFs) envelopes in natural logarithmic scale for the first three fundamental modes in the east-west (EW) direction. The data correspond to the mainshock EW direction. For the first mode, curves between 2.0 and 20.0 s; for the second mode, curves between 0.5 and 10.0 s; and for the third-mode curves between 0.5 and 5.0 s are fitted with a straight line using least squares to find the slope. The measured slope yields a quality factor ($Q = -\pi f/slope$, f = predominant frequency) of 12.5 for the first mode, 19.6 for the second mode, and 9.3 for the third mode. The color version of this figure is available only in the electronic edition.

The records at different floors were deconvolved with the records obtained from the first floor to generate causal IRFs. The IRFs were then bandpass filtered around the resonant frequencies using a second-order acausal Butterworth filter with corner frequencies of 0.2 and 1.0 Hz for the first, 1.0 and 2.0 Hz for the second, and 2.0 and 3.0 Hz for the third-mode.

The natural logarithm of the envelopes of the bandpass-filtered waveforms corresponding to the mainshock is depicted in Fig. 14. In order to separate the curves at different heights, an offset equal to the floor number is added to the natural logarithm of the envelope. The slope of the curves depends on the wave attenuation; thus, the offset has no effect on the results. The slopes of the curves, which are similar at different floors, were calculated in the least square sense between t_1 and t_2. The decay of the natural logarithm of the envelope follows the rule between t_1 and t_2, defined by Eq. (5), while the exponential decay is not valid for the later times (Snieder and Şafak 2006). The values of t_1 and t_2 are determined by inspecting the deconvolved waveforms of different earthquakes. The slope of the fitted line is equal to $-\pi f/Q$. The consistency of slope for different floors indicates the consistency of Q values for different floors.

The average slope at different layers, generally consistent at different floors, and the first mode frequencies identified with the CMIF method (see Table 3) were used to determine the average Q and ξ. Table 5 summarizes the results for all earthquakes. We interpret the damping primarily as that of the building because of the insignificant foundation rocking observed during all earthquakes studied here, which curtails the contribution of radiation damping. The variability of the damping ratio is moderate with a coefficient of variation of 14% and 12% for the EW and NS directions, respectively. The average damping ratio for the fundamental modes is found to be 4.4% and 3.7% in the EW and NS directions, respectively. The EW damping value is 18.9% more than the NS damping value, and this difference is larger than the previous results obtained by investigating events between 2005 and 2014 (Wen and

Table 5. Mean slope of different layers, quality factor Q, and intrinsic-damping ratio ξ (in percentage) computed for different earthquakes.

	East-West			North-South		
Event No.	Slope	Q	ξ (%)	Slope	Q	ξ(%)
1	−0.09	12.81	3.9	−0.11	12.46	4.0
2	−0.13	9.72	5.1	−0.15	11.04	4.5
3	−0.13	9.51	5.3	−0.11	14.99	3.3
4	−0.14	10.70	4.7	−0.12	14.17	3.5
5	−0.11	12.85	3.9	−0.11	15.50	3.2
6	−0.10	12.91	3.9	−0.13	12.75	3.9
7	−0.12	12.78	3.9	−0.12	14.19	3.5
Average		11.61	4.4		13.59	

Kalkan 2017). Kashima (2017) used a different method to identify the damping ratios of other four high-rise buildings, and the results are clearly lower than the results here, which may due to the different structural features among different buildings. The values of damping ratios identified here are generally consistent with the results from the previous events (Çelebi 2006; Wen and Kalkan 2017), indicating that there is no clear structural damage occur in this building.

6. Conclusions

The deconvolution is applied to the waveform data recorded in a twenty-story structure in Anchorage, Alaska, during the M7.1 Anchorage earthquake sequence. The waveform data from a 32-channel accelerometer array include accelerations observed from the mainshock and six aftershocks. The data are used to compute the impulse response functions (IRFs) based on deconvolution, which led to the estimation of velocities of traveling waves and intrinsic damping. The building's fundamental frequencies and mode shapes are obtained by using a complex mode indicator function (CMIF) based on singular value decomposition of multiple reference frequency-response functions. The dynamic characteristics of this building identified are compared with those retrieved from previous earthquakes between 2005 and 2014. The key findings of this study are as follows:

(1) The median shear-wave velocities identified from the IRFs of the seven earthquakes are 179 m/s for the east-west (EW), 201 m/s for the north-south (NS), and 174 m/s for the torsional responses. The median shear-wave velocities along the EW direction are in general 10% less than those along the NS direction because the averaged stiffness of the building along the NS direction is slightly larger than that along the EW direction. The shear-wave velocities identified from this earthquake sequence are close to the results obtained from the earlier events with a difference of about 7%.

(2) The average values of the fundamental frequency (first-mode) from seven earthquakes are 0.43, 0.51, and 0.52 Hz, respectively, for the EW, NS, and torsional responses. The relative difference between the largest and lowest frequencies can exceed 20%, which is moderately higher than those identified based on the events from 2005 to 2014, mainly due to the fact that the mainshock induces more significant non-structural damage.

(3) The modal assurance criterion (MAC) and curvature mode shapes demonstrate that the change in the mode shapes is insignificant as compared to the change in the frequencies, which is consistent with the results obtained from earlier events. We interpret a change in shear-wave velocities (and frequencies) that we observe during the stronger event as due to the opening and closing of gaps between non-structural and structural components.

(4) The damping ratios identified are consistent among the seven earthquakes with a coefficient of variation of 14% and 12% for the EW and NS directions, respectively. The building's average intrinsic-damping ratio is estimated to be 4.4% and 3.7% in the 0.2–1 Hz band for

the EW and NS directions, respectively. The EW damping value is 18.9% more than the NS damping value, and this difference is larger than the previous results obtained from events 2005 to 2014.

Acknowledgments

Disclosure statement

Data and Resources

The data, models, or codes generated or used during the study are available from the corresponding author by request. Instruments of the National Strong Motion Network of USGS collected recordings used in this study. These recordings are available at http://nees.ucsb.edu/data-portal (last accessed Jan. 2021). Figure 2 is adapted from https://earthquake.usgs.gov/monitoring/nsmp/arrays/schematics/8040.pdf (last accessed April 2021). The MATLAB version of the deconvolution function used in this study is available at https://www.mathworks.com/matlabcentral/fileexchange/60644-deconvolution-of-two-discrete-time-signals-in-frequency-domain?s_tid=prof_contriblnk.

ORCID

Weiping Wen 🆔 http://orcid.org/0000-0001-9354-344X

References

Aki, K., and P. G. Richards. 2002. *Quantitative seismology.* Mill Valley, CA: University Science Books.
Allemang, R. J. 2003. The modal assurance criterion-twenty years of use and abuse. *Sound and Vibration* 37 (8): 14–23.
Allemang, R. J., and D. L. Brown. 1982. A correlation coefficient for modal vector analysis. 1st International Modal Analysis Conference, vol. 1, 110–16. Orlando: SEM.
Allemang, R. J., and D. L. Brown. 2006. A complete review of the complex mode indicator function (CMIF) with applications. Proceedings of ISMA2006 Int. Conference on Noise and Vibration Engineering, 3209–46. Leuven, Belgium.
Boutin, C., S. Hans, E. Ibraim, and P. Roussillon. 2005. In situ experiments and seismic analysis of existing buildings. Part II: Seismic integrity threshold. *Earthquake Engineering & Structural Dynamics* 34: 1531–46. doi: 10.1002/eqe.503.
Çelebi, M. 2006. Recorded earthquake responses from the integrated seismic monitoring network of the Atwood building, Anchorage, Alaska. *Earthquake Spectra* 22 (4): 847–64. doi: 10.1193/1.2359702.
Ebrahimian, M., and M. I. Todorovska. 2014. Wave propagation in a Timoshenko beam building model. *Journal of Engineering Mechanics* 140 (5): 04014018. doi: 10.1061/(ASCE)EM.1943-7889.0000720.
Ebrahimian, M., and M. I. Todorovska. 2015. Structural system identification of buildings by a wave method based on a non-uniform Timoshenko beam model. *Journal of Engineering Mechanics* 141: 04015022. doi: 10.1061/(ASCE)EM.1943-7889.0000933.
International Conference of Building Officials. 1979. Uniform building code. Whittier, CA.
Jibson, R. W., A. R. R. Grant, R. C. Witter, K. E. Allstadt, E. M. Thompson, and A. M. Bender. 2020. Ground failure from the Anchorage, Alaska, earthquake of November 30, 2018. *Seismological Research Letters* 91: 19–32. doi: 10.1785/0220190187.
Kalkan, E., and W. Wen. 2017. Dynamic characteristics of a twenty-story instrumented building in Anchorage, Alaska identified by seismic interferometry. *16th World Conference on Earthquake Engineering*, Santiago, Chile, Paper no. 453.

Kalkan, E., W. Wen, and Y. Heo. 2021. Delaney park geotechnical array dynamic properties inferred from the magnitude 7.1 2018 Anchorage, Alaska, earthquake sequence. *Journal of Geotechnical and Geoenvironmental Engineering* 147 (1): 04020150. doi: 10.1061/(ASCE)GT.1943-5606.0002413.

Kashima, T. 2017. Study on changes in dynamic characteristics of high-rise steel framed buildings based on strong motion data. *Procedia Engineering* 199: 194–99. doi: 10.1016/j.proeng.2017.09.269.

Kohler, M. D., T. H. Heaton, and S. C. Bradford. 2007. Propagating waves in the steel, moment-frame factor building recorded during earthquakes. *Bulletin of the Seismological Society of America* 97 (4): 1334–45. doi: 10.1785/0120060148.

Nakata, N., and R. Snieder. 2014. Monitoring a building using deconvolution interferometry. II: Ambient-vibration analysis. *Bulletin of the Seismological Society of America* 104 (1): 204–13. doi: 10.1785/0120130050.

Nakata, N., R. Snieder, S. Kuroda, S. Ito, T. Aizawa, and T. Kunimi. 2013. Monitoring a building using deconvolution interferometry. I: Earthquake-data analysis. *Bulletin of the Seismological Society of America* 103 (3): 1662–78. doi: 10.1785/0120120291.

Nakata, N., W. Tanaka, and Y. Oda. 2015. Damage detection of a building caused by the 2011 Tohoku-Oki earthquake with seismic Interferometry. *Bulletin of the Seismological Society of America* 105 (5): 2411–19. doi: 10.1785/0120140220.

Newton, C., and R. Snieder. 2012. Estimating intrinsic attenuation of a building using deconvolution interferometry and time reversal. *Bulletin of the Seismological Society of America* 102 (5): 2200–08. doi: 10.1785/0120110322.

Pastor, M., M. Binda, and T. Harčarik. 2012. Modal assurance criterion. *Procedia Engineering* 48: 543–48. doi: 10.1016/j.proeng.2012.09.551.

Prieto, G. A., J. F. Lawrence, A. I. Chung, and M. D. Kohler. 2010. The impulse response of civil structures from ambient noise analysis. *Bulletin of the Seismological Society of America* 100 (5A): 2322–28. doi: 10.1785/0120090285.

Rades, M. 2010. Performance of various mode indicator functions. *Shock and Vibration* 17: 473–82. doi: 10.1155/2010/546802.

Rahmani, M., M. Ebrahimian, and M. I. Todorovska. 2015. Wave dispersion in high-rise buildings due to soil-structure interaction. *Earthquake Engineering & Structural Dynamics* 44 (2): 317–23. doi: 10.1002/eqe.2454.

Rahmani, M., and M. I. Todorovska. 2013. 1D system identification of buildings from earthquake response by seismic interferometry with waveform inversion of impulse responses-method and application to Millikan Library. *Soil Dynamics and Earthquake Engineering* 47: 157–74. doi: 10.1016/j.soildyn.2012.09.014.

Rodgers, J., W. Hassan, C. Motter, and J. Thornley. 2021. Impacts of the 2018 M7.1 Anchorage earthquake on schools. *Earthquake Spectra* 37 (3): 1849–74. doi: 10.1177/8755293020988022.

Roux, P., P. Guéguen, L. Baillet, and A. Hamze. 2014. Structural-change localization and monitoring through a perturbation-based inverse problem. *The Journal of the Acoustical Society of America* 136 (5): 2586–97. doi: 10.1121/1.4897403.

Ruppert, N. A., A. Nayak, C. Thurber, and C. Richards. 2020. Aftershock analysis of the 2018 Mw 7.1 Anchorage, Alaska, earthquake: Relocations and regional moment tensors. *Seismological Research Letters* 91: 114–25. doi: 10.1785/0220190199.

Ruppert, N. A., and R. C. Witter. 2020. Preface to the focus section on the November 30, 2018 Mw 7.1 Anchorage, Alaska, earthquake. *Seismological Research Letters* 91: 16–18. doi: 10.1785/0220190344.

Shih, C. Y., Y. G. Tsuei, R. J. Allemang, and D. L. Brown. 1988. Complex mode indication function and its applications to spatial domain parameter estimation. *Mechanical Systems and Signal Processing* 2 (4): 367–77. doi: 10.1016/0888-3270(88)90060-X.

Snieder, R., and E. Şafak. 2006. Extracting the building response using seismic interferometry: Theory and application to the Millikan library in Pasadena, California. *Bulletin of the Seismological Society of America* 96 (2): 586–98. doi: 10.1785/0120050109.

Stein, R. S., J. R. Patton, and V. Sevilgen. 2018. Exotic M=7.0 earthquake strikes beneath Anchorage, Alaska. Accessed August, 2019. http://temblor.net/earthquake-insights/exotic-m7-0-earthquake-strikes-beneath-anchorage-alaska-8010/ .

Todorovska, M. I. 2009. Seismic interferometry of a soil-structure interaction model with the horizontal and rocking response. *Bulletin of the Seismological Society of America* 99 (2A): 611–25. doi: 10.1785/0120080191.

Todorovska, M. I., and M. T. Rahmani. 2013. System identification of buildings by wave travel time analysis and layered shear beam models—spatial resolution and accuracy. *Structural Control and Health Monitering* 20: 686–702. doi: 10.1002/stc.1484.

Vasconcelos, I., and R. Snieder. 2008. Interferometry by deconvolution: Part 1—Theory for acoustic waves and numerical examples. *Geophysics* 73 (3): S115–S128. doi: 10.1190/1.2904554.

Wen, W., and E. Kalkan. 2017. System identification based on deconvolution and cross-correlation: An application to a 20-story instrumented building in Anchorage, Alaska. *Bulletin of the Seismological Society of America* 107 (2): 718–40. doi: 10.1785/0120160069.